Notice

Manuscript details

Title: Kathmandu Basin as a local modulator of seismic waves: 2-D modelling of non-linear site response under obliquely incident waves

Authors: Elif Oral (Caltech and Geoazur), Peyman Ayoubi, Jean-Paul Ampuero, Domniki Asimaki, and Luis Fabian Bonilla

Contact: elifo@caltech.edu

Geophysical Journal International

Geophys. J. Int. (2022) **231,** 1996–2008
Advance Access publication 2022 August 6
GJI Seismology

https://doi.org/10.1093/gji/ggac302

Kathmandu Basin as a local modulator of seismic waves: 2-D modelling of non-linear site response under obliquely incident waves

Elif Oral [1,2] Peyman Ayoubi,[2] Jean Paul Ampuero [1] Domniki Asimaki[2] and Luis Fabian Bonilla [3]

[1] *Université Côte d'Azur, IRD, CNRS, Observatoire de la Côte d'Azur, Géoazur, 06560 Valbonne, France. E-mail: elifo@caltech.edu*
[2] *Mechanical and Civil Engineering, California Institute of Technology, Pasadena CA 91125, USA*
[3] *Geotechnical Engineering, Environment, Natural hazards and Earth sciences Department, Université Gustave Eiffel, 77447 Marne-la-Vallée Cedex 2, France*

Accepted 2022 August 3. Received 2022 April 30; in original form 2021 October 10

SUMMARY

The 2015 M_w 7.8 Gorkha, Nepal earthquake is the largest event to have struck the capital city of Kathmandu in recent times. One of its surprising features was the frequency content of the recorded ground motion, exhibiting a notable amplification at low frequencies (<2 Hz) and a contrasting depletion at higher frequencies. The latter has been partially attributed to the damper behaviour of the Kathmandu basin. While such weak high-frequency ground motion helped avoiding severe damage in the city, the catastrophic outcomes of earlier earthquakes in the region attest to a contrasting role of the Kathmandu basin as a broad-band amplifier, in addition to possible source effects. Given the possibility of future strong events in the region, our main objective is to elucidate the seismic behaviour of the Kathmandu basin by focusing on site effects. We numerically model 2-D *P–SV* wave propagation in a broad frequency band (up to 10 Hz), incorporating the most recent data for the Kathmandu basin geometry, soil stratigraphy and geotechnical soil properties, and accounting for the non-linear effect of multidimensional soil plasticity on wave propagation. We find that: (1) the Kathmandu basin generally amplifies low frequency ground motion (<2 Hz); (2) waves with large incidence angles relative to vertical can dramatically amplify the high frequency ground motion with respect to bedrock despite the damping effect of soil non-linearity and (3) the spatial distribution of peak ground motion amplitudes along the basin is highly sensitive to soil non-linearity and wave incidence (angle and direction), favouring larger values near the basin edges located closer to the source, as observed during the 2015 event. Our modelling approach and findings can support the ongoing resilience practices in Nepal and can guide future seismic hazard assessment studies for other sites that feature similar complexities in basin geometry, soil stratigraphy and dynamic soil behaviour.

Key words: Elasticity and anelasticity; Asia; Numerical modelling; Earthquake ground motions; Site effects; Wave propagation.

1 INTRODUCTION

The 25 April 2015 Gorkha, Nepal earthquake (magnitude 7.8) was the largest event to hit the capital city of Kathmandu in recent times, yet seismic hazard in the region remains high (e.g. Avouac *et al.* 2015; Galetzka *et al.* 2015; Rajaure *et al.* 2017). The rupture broke the bottom portion of the locked zone of an eastern segment of the Main Himalayan Thrust (MHT; Avouac *et al.* 2015; Zhang *et al.* 2016). Kathmandu is located within 80 km of the epicentre. Within a month, two M 6+ aftershocks occurred (magnitudes 6.7 and 6.8) in the southeast of the main shock epicentre. The following day, the strongest aftershock of magnitude 7.3 occurred east of Kathmandu, near Dolakha, and was followed by a M 6.2 aftershock in its proximity (Fig. 1a). The ruptures during this sequence of five events did not reach to shallower parts of the fault. The possibility of stress transfer to the unbroken shallower portion of the fault and the long-known seismic gap in the western part of the MHT underline the likelihood of another M 7+ megathrust event in the area (Avouac *et al.* 2015; Dal Zilio *et al.* 2019).

The seismic response of the Kathmandu basin during the Gorkha event was particular: ground motion was notably weak at high frequencies and enhanced at low frequencies compared to empirical expectations (e.g. Galetzka *et al.* 2015; Takai *et al.* 2016; Asimaki *et al.* 2017; Rajaure *et al.* 2017). The recorded amplitudes at the stations of the Kathmandu Valley were below the estimations of ground motion prediction equations (GMPE) at frequencies higher

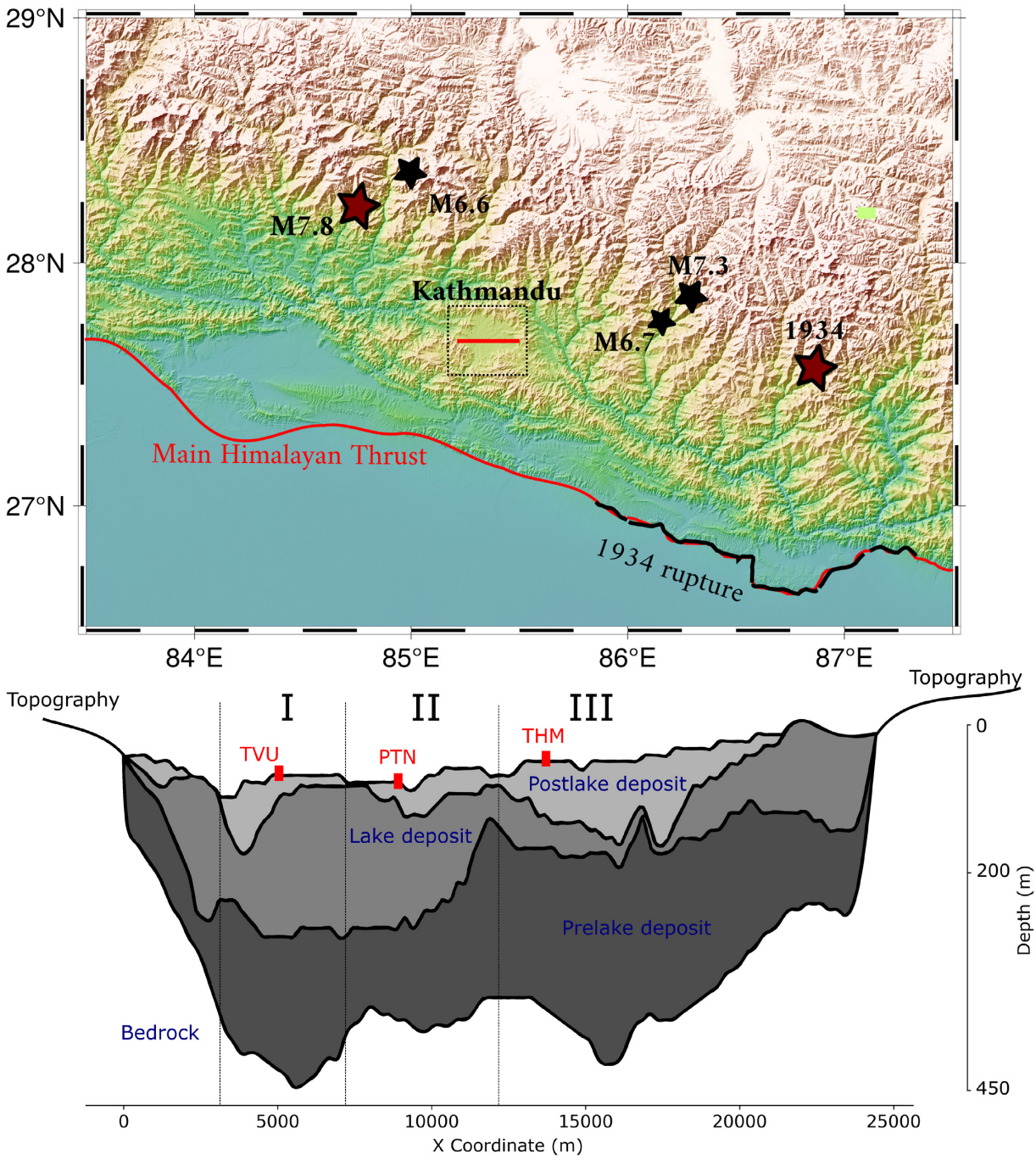

Figure 1. Overview of the 2015 Gorkha, Nepal earthquake sequence and Kathmandu basin. Top panel: epicentres of the selected past earthquakes (stars), surface trace of the Main Himalayan Thrust (red curve), lateral extension of the 1934 rupture (black curve), and location of the Kathmandu basin (black dashed square, with the red line indicating the 2-D cross-section). Bottom panel: detailed view of the 2-D basin model, with vertical axis scaled 10 times for better visualization. Red squares indicate the locations of seismic stations.

than about 2 Hz (Hough *et al.* 2016; Rajaure *et al.* 2017). Since such weakness of high-frequency ground motion was observed at both rock and soil stations, it is mainly associated with source effects, namely a deficiency of high-frequency radiation by the earthquake rupture in the proximity of the basin (Michel *et al.* 2017) and a complex rupture geometry (Wang *et al.* 2019). Soil non-linearity is an additional factor that could have led to further attenuation of high-frequency ground motion inside the basin, and is a subject of this work. Ground motion amplification by the basin, quantified by peaks in the basin-to-rock spectral ratios of ground motion, was observed to occur at lower frequencies during the strongest events of the sequence (M 7.8 Gorkha main shock and M 7.3 Dolakha aftershock) than during the weaker aftershocks. This observation was interpreted as a reduction of the resonance frequency of the basin induced by soil non-linearity (e.g. Asimaki *et al.* 2017; Rajaure *et al.* 2017).

On the other hand, low-frequency ground motion in Kathmandu was enhanced due to site effects controlled by the basin geometry

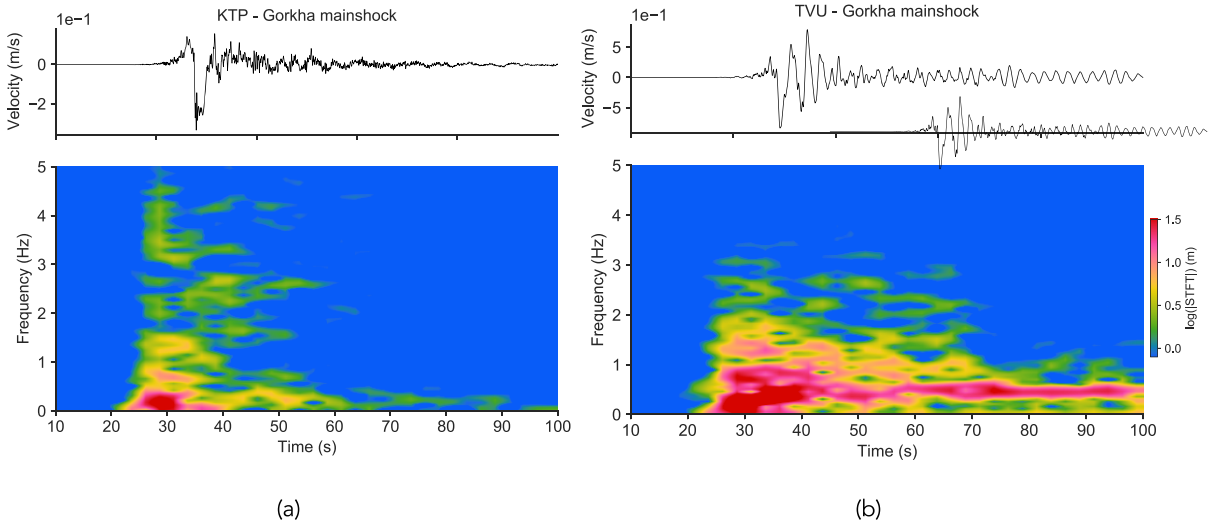

Figure 2. Ground motion recordings of the 2015 Gorkha earthquake at rock and soil stations. East–west ground velocity time histories (top panel) and short-time Fourier transform spectogram (bottom panel) for the rock station KTP (a) and the soil station TVU (b). Origin time is 2015-04-25 06:11:25.95.

and soil stratigraphy. A striking difference between the recordings of rock and soil stations is the prolonged ground motion at the soil stations at low frequencies, on the order of 40 s longer. This difference is exemplified in Fig. 2 by comparing the recordings of a rock station (KTP) and a soil station (TVU) that are separated by less than 1 km—short enough to ignore differences in source effects. Moreover, during all the events of the Gorkha sequence, the ground motion Fourier spectra below ∼2 Hz at soil stations were up to five times larger than at rock stations, which is an indication of site effects of the Kathmandu basin (e.g. Rajaure *et al.* 2017). The amplification of ground motion at low frequencies due to basin resonance is indeed a well-recognized phenomenon that has been reported for many areas, such as Seattle, USA (Frankel *et al.* 2002), L'Aquila, Italy (De Luca *et al.* 2005) and Quito, Ecuador (Laurendeau *et al.* 2017) and Los Angeles, USA (Olsen 2000). A detailed discussion on the physics of site effects and the evolution of site effects studies can be found in Bard *et al.* (1995) and Ayoubi *et al.* (2021).

Concerning high-frequency ground motion, Kathmandu basin may have played a contrasting role during past earthquakes. Prior to the 2015 earthquake, severe seismic vulnerability was reported for the structures in the Kathmandu Valley (Jica 2002; Dixit *et al.* 2013). The weakness of the high-frequency ground motion during the Gorkha sequence, which was partially due to the basin non-linearity as discussed above, was a fortunate feature: it may have prevented further damages in Kathmandu. Damage was not severe on residential structures, which are commonly reinforced concrete buildings with masonry infills, mostly three to four stories high, and sensitive to higher frequencies than high-rise buildings (Chiaro *et al.* 2015; Hashash *et al.* 2015; Kaushik *et al.* 2016). By contrast, available documentation on earlier earthquakes points to extensive and much higher human and damage tolls (e.g. Sapkota *et al.* 2013; Dixit *et al.* 2013). For example, the 15 January 1934 earthquake, which likely had a magnitude of M_w 8.1–8.2, caused great destruction and 11 000 deaths (Auden & Ghosh 1935; Singh & Gupta 1980). Its extensive damage in Kathmandu was possibly due to strong amplification inside the basin (e.g., Hough & Roger 2008). Similar outcomes were also reported for the 1255 earthquake (e.g. Sapkota *et al.* 2013). In light of such a contrast between the impact of different earthquakes on Kathmandu, and given the poor construction practice (e.g. Dixit *et al.* 2013), we hypothesize a stronger high-frequency ground motion for the events before the Gorkha earthquake.

Given the high seismic hazard and the possible disparity of the Kathmandu basin behaviour in the past, we primarily address the following question: What seismic response of the Kathmandu basin should we expect during future earthquakes—possibly a different frequency content or spatial distribution than during the Gorkha earthquake? To answer this question, we here focus on site effects: despite possibly short source-to-site distance, we ignore complexities arising from fault finiteness by limiting our study to the assumption of plane wave incidence. We numerically model the 2-D broad-band seismic response of the Kathmandu basin for linear and non-linear soil behaviour and different wave incidences. Previous numerical modelling of the Gorkha earthquake supported that the Kathmandu basin can enhance low frequency ground motion (Ayoubi *et al.* 2018; Wei *et al.* 2018) and attenuate high frequency ground motion by soil non-linearity (Ayoubi *et al.* 2018; Chen & Wei 2019), but these studies were based on substantial simplifications, notably simplified basin geometry and soil stratigraphy and 1-D modelling of soil non-linearity. Here we take these initial efforts a step further, by considering a realistic basin structure and geotechnical soil properties, obtained by a recent geotechnical survey (SAFER, Gilder *et al.* 2020), together with a 2-D non-linear modelling approach that couples 2-D basin effects and multidimensional soil plasticity (Oral *et al.* 2019). Previous work showed that the amplification of ground motion due to basin effects can be severely damped by soil non-linearity (Marsh *et al.* 1995; Psarropoulos *et al.* 2007; Roten *et al.* 2014; Esmaeilzadeh *et al.* 2019), yet a 1-D wave propagation modelling approach underestimates the ground motion even when soil non-linearity is triggered (Ragozzino 2014; Chen *et al.* 2015; Oral *et al.* 2019). Moreover, 2-D and 3-D wave propagation effects also enhance non-linearity when multidimensional soil plasticity is considered, compared to 1-D plasticity, which can affect final surface displacement (e.g., Oral *et al.* 2017). Thus the consideration of multidimensional soil plasticity is necessary for a robust estimation of ground motion amplitudes. In addition, as reported in earlier studies on simplified 2-D basin models, wave incidence angle can significantly impact the amplitude, duration and spatial distribution of ground motion (Liu *et al.* 1991;

Table 1. Soil properties of the Kathmandu basin model.

Layer	Soil type	Density	V_p (m s^{-1})	V_s (m s^{-1})	Q_p	Q_s
Postlake deposit	Fine to medium sand and silt	1600	416.33	200	40	20
Lake deposit	Clay	1800	810.00	425	80	40
Prelake deposit	Gravel and sand	2000	2298.40	1250	230	125
Bedrock	Precambrian to Devonian rocks	2530	5500.00	3200	300	150

Papageorgiou & Kim 1993; Bonilla *et al.* 2011; Zhu *et al.* 2016; Zhang *et al.* 2017). Site-specific features, such as surface topography, irregular geometry of layer interfaces and asymmetry of basin geometry, can further contribute to variability of ground motion across the basin (e.g. Ragozzino 2014) and are not well captured by 1-D modelling approaches. Given that the Kathmandu basin is surrounded by active faults and is not symmetrical, we also investigated the sensitivity of the ground motion inside the Kathmandu basin to the obliquity of incident waves.

In the following, we first present the studied area, and the methods and data used for numerical modelling. Then, we report our results on site effects in the Kathmandu basin at low and high frequencies. Next, we discuss the spatial variation of ground motion along the Kathmandu basin. Last, we summarize our main findings and perspectives for future research.

2 METHODS AND SITE PROPERTIES

Kathmandu is located on an intermontane basin in the midland of the Lesser Himalayas (Sakai *et al.* 2002). Here we study a 2-D east-west cross-section that extends in the east–west direction. We first created the 3-D geometry of the Kathmandu basin by combining the subsurface images of Piya (2004) with geotechnical data. Piya (2004) developed a database of subsurface geometry for liquefaction hazard assessment; we processed these images with the geotechnical dataset of SAFER (Gilder *et al.* 2020) and obtained a 3-D model of the basin geometry. For the numerical models in this study, we selected a 2-D cross-section that covers the locations of the stations that were deployed by Takai *et al.* (2016), as indicated by the red line in Fig. 1(a).

We set three sediment layers for the basin and consider that the shallowest layer is non-linear. Fig. 1(b) displays the geometry of the layers in our 2-D section. The deepest part is mostly filled with sand and gravel; the middle part is mainly clay; and the shallowest part is made of fine-to-medium sand, and silt intercalated with clays (Sakai 2001). Outside the basin, basement rock is formed by Precambrian to Devonian rocks. In accordance with this knowledge, we set three types of basin soil: Bagmati (pre-lake deposit), Kalimati (lake deposit) and Patan (post-lake deposit). The basin model has a length of 24.4 km and a maximum depth of about 450 m in the central part. We referred to the recent geotechnical project SAFER (Gilder *et al.* 2020) while setting up the soil properties in the 2-D Kathmandu basin model, listed in Table 1. We used a depth-averaged velocity profile after Ayoubi *et al.* (2018, 2021) that is derived from this geotechnical data and captures well the 2-D basin effects in elastic modelling. To simplify the evaluation in the following, we virtually divided the basin into three sections, referred to hereafter as the western, middle and eastern parts of the basin, respectively, as denoted by I, II and III in Fig. 1(b).

In the absence of detailed knowledge of soil non-linearity properties, we assumed that only the first layer is non-linear, given its soil type, relatively shallow depth and low velocity. We set a cohesion and friction angle of 20 kPa and 10°, respectively. We verified our choice by determining soil non-linearity properties, mainly the backbone curve, from the shift of resonance frequencies observed during strong events (Rajaure *et al.* 2017), by applying the method of Castro-Cruz *et al.* (2020) to the ground motion recordings of the Gorkha sequence (detailed in SI). In our models, the overburden (or effective) stress increases with depth, such that the backbone curve varies with depth inside the non-linear layer. With our choice of non-linearity parameters, the mid-layer has a backbone curve consistent with the one obtained by frequency-shift analysis, as shown in Fig. S1. We also verified that varying the level of soil non-linearity—by setting a different friction angle, the most determinant parameter of the backbone curve that describes non-linear soil behaviour in our model—does not change the conclusions of our study (detailed in Section S1 of Supplementary Information). In addition to soil non-linearity, for all layers, we considered viscoelastic attenuation by setting quality factors that approximately equal 10 per cent of the velocity values, as shown in the table, after Olsen *et al.* (2003) and Régnier *et al.* (2018) in the absence of local data. We denote the viscoelastic cases as 'linear' cases throughout the manuscript. Soil non-linearity is based on the viscoelastoplasticity implementation of Oral (2016); Oral *et al.* (2017), such that the non-linear soil behaviour gets closer to viscoelastic response at lower strains.

We numerically modelled seismic wave propagation in linear and non-linear media in 2-D with *P-SV* polarization (in-plane). We used the spectral element method (e.g. Komatitsch & Vilotte 1998; Chaljub *et al.* 2007) implemented in the software SEM2DPACK for 2-D seismic wave propagation (Ampuero *et al.* 2002; Ampuero 2012) including soil non-linearity (Oral *et al.* 2019; see 'Data and Resources' section for software availability). The implemented model of soil non-linearity follows the Iwan (1967) method and is based on the formulation of Joyner (1975), as detailed in Oral *et al.* (2019). To achieve a good resolution of the wavefield up to 10 Hz, accounting for possible velocity reduction due to soil non-linearity, we set the element size such that the node spacing ranges between 0.2 and 85 m. We prepared an unstructured mesh with the CUBIT mesh generation software. The mesh is made of conforming elements that follow the material interfaces. In particular, the size of elements at an interface is dictated by the material with lower wave speed, to satisfy the minimum-wavelength resolution criterion. The time step equals 1.5×10^{-4} s. We set the boundary conditions as periodic on the sides, free surface on top, and absorbing (Clayton & Engquist 1977) at the bottom, for the vertical incidence. For oblique incidence, we again use free surface on top, and absorbing layers elsewhere. The incident wave field enters through the absorbing layers, as in Oral *et al.* (2019), following the formulation of Delavaud *et al.* (2006). We verified for both vertical and oblique incidence cases that our model set-up satisfactorily works to avoid artificial reflections from boundaries towards the basin. We use the leap-frog scheme for time discretization and set the time step to satisfy a Courant–Friedrichs–Lewy (CFL) condition with Courant number ≤ 0.3.

We analysed different levels of triggered soil non-linearity by comparing the basin response to two different input motions with

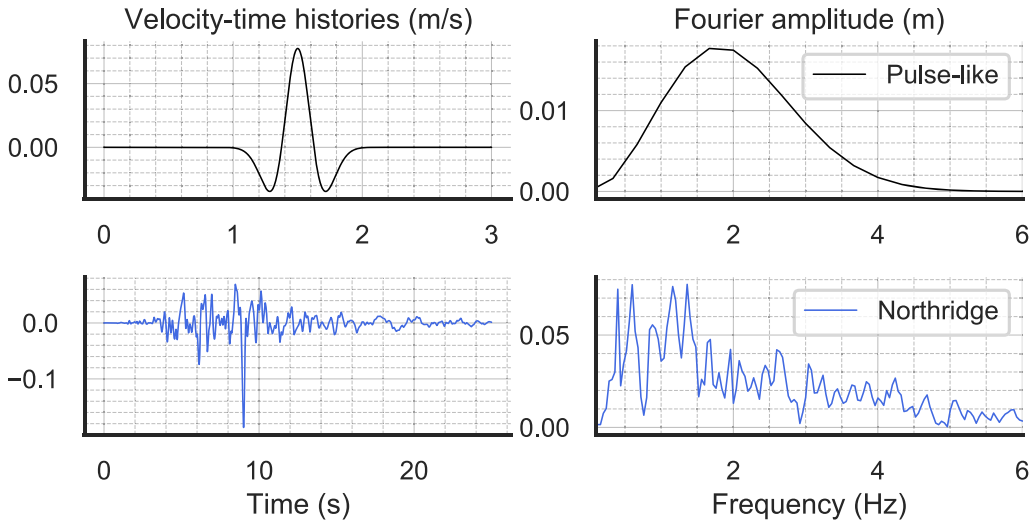

Figure 3. Input motions used in the simulations. Velocity–time histories (left-hand panel) and Fourier amplitude (right-hand panel) for the pulse-like input (top panel) and the Northridge input (bottom panel).

same amplitude but contrasting waveform complexity. Triggered soil non-linearity is known to correlate with the peak amplitude of input motion: a dynamic loading with a larger peak acceleration generally induces larger plastic strain. In addition, the complexity of the input motion, qualified by the number of loading-unloading cycles, also affects the level of soil non-linearity (Gélis & Bonilla 2012). This implies that stronger non-linearity can be expected for input time histories with more zero-crossings. Thus, we prepared two input motions, with the same peak acceleration of 0.1 g—simply by scaling their amplitude—but with a contrasting level of complexity: a smooth pulse-like input motion made of a Ricker wavelet with zero-crossings (hereafter referred to as 'pulse-like' input) and a real input motion based on the recording of the 1994 Northridge earthquake at LA00 station in the east-west direction (hereafter referred to as 'Northridge' input). Fig. 3 displays their velocity-time histories and corresponding Fourier amplitudes. Both inputs have sufficiently high energy below 5 Hz, and the Northridge spectrum peaks at half lower frequency (∼1 Hz) than the pulse-like spectrum.

3 RESULTS

3.1 Kathmandu Basin typically enhances the low-frequency ground motion (<2 Hz)

We find that the Kathmandu Basin can amplify low-frequency ground motion with and without soil non-linearity. Fig. 4(a) displays the site-to-rock spectral ratios along the basin length for linear and non-linear models up to 4 Hz, the upper frequency at which the input motions have substantial energy (Fig. 3). We used the geometric mean of the fast Fourier amplitudes of ground motion at rock stations when calculating the spectral ratios throughout this study. To isolate the effect of rheology, we considered vertically incident plane waves. In the linear model, the spectral ratios reach values around 8 inside the basin, in particular below 2 Hz. We find fundamental frequencies in the range of 0.3–1.5 Hz. The largest spectral ratios correspond to about 0.5 Hz mostly in the central basin sections. Spatial variations to higher values are present near local basin edges as expected given the irregularities of the basin geometry and layer interfaces, and the rough topography near the basin edges (Fig. 1b). Our frequency range is in agreement with the 0.1–2.5 Hz range reported in the observational studies on the Gorkha earthquake cited above. Potential reasons for the reported frequencies below 0.3 Hz and above 1.5 Hz can be the 3-D effects (coupling of *P–SV* and *SH* waves), geometrical features at surface and depth that are not represented in our 2-D cross-section, and a spatial variability of the presence of non-linear layers and triggered non-linearity in contrast to our assumption that only the 1st layer is non-linear. Investigating whether the inclusion of these factors can capture the reported frequency range of basin resonance is of interest for further studies on Kathmandu. Consideration of basin non-linearity notably reduces the spectral ratios for both input motions. However, the spectral amplification around the fundamental frequency persists. Thus, the Kathmandu Basin can enhance low-frequency ground motion, as observed during the Gorkha earthquake, for both linear and non-linear basin rheologies.

Pronounced low-frequency ground motion in the Kathmandu Basin also occurs under oblique wave incidence. In Fig. 5, we present the soil-to-rock spectral ratios for three wave incidence angles relative to the vertical axis: 30° from west, 0° and 30° from east. An incidence of 30° is plausible for the regional seismotectonics and useful for comparison purposes. We used the Northridge input and considered soil non-linearity in all the three cases. The change of incidence angle causes local variations in the fundamental frequencies and spatial pattern of the spectral ratios. If incidence is from west (east), the largest amplification appears in the western (eastern) side of the basin. In all cases, the largest soil-to-rock spectral ratios occur at low frequencies, below 2 Hz, which corroborates the amplification of low frequency ground motion by the Kathmandu basin effects.

3.2 Oblique wave incidence can boost high frequency ground motion despite soil non-linearity

Soil non-linearity causes ground motion damping and local reduction of fundamental frequencies for the input motions used here. To evaluate how the soil non-linearity can affect the wave propagation in the basin, we evaluated the soil-to-rock spectral ratios of the non-linear cases with pulse-like and Northridge inputs (Fig. 4). Both

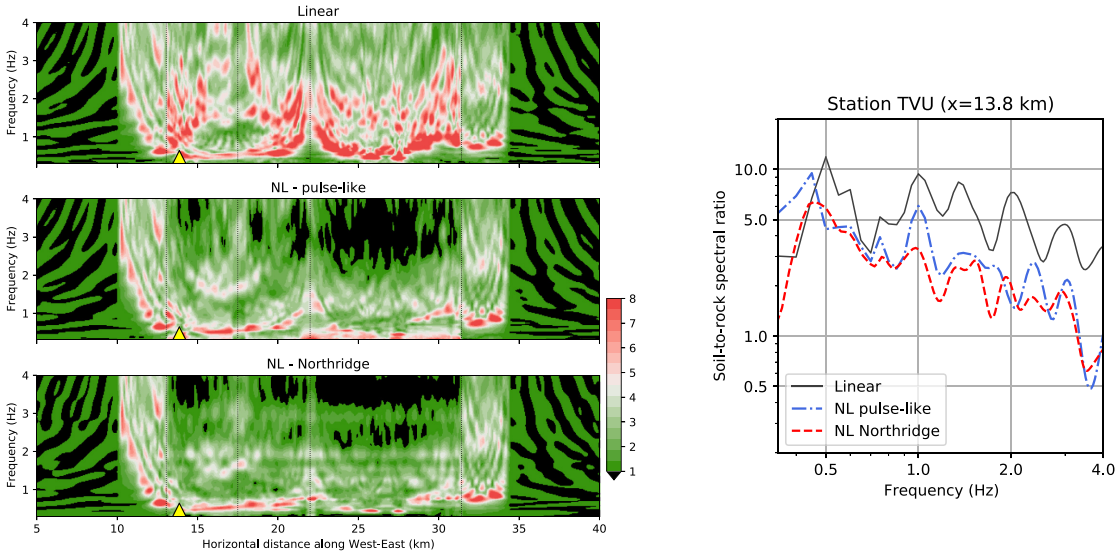

Figure 4. Site-to-rock spectral ratios for different soil rheologies. Left-hand panel: 2-D spectral ratios for a viscoelastic model (top panel) and non-linear models with pulse-like input (middle panel) and Northridge input (bottom panel). Right-hand panel: spectral ratios of the three models at the location of station TVU (yellow triangle on the left plots). Wave incidence is vertical in the three cases. Outer and inner dashed lines indicate the basin-bedrock limits and inner basin sections, respectively.

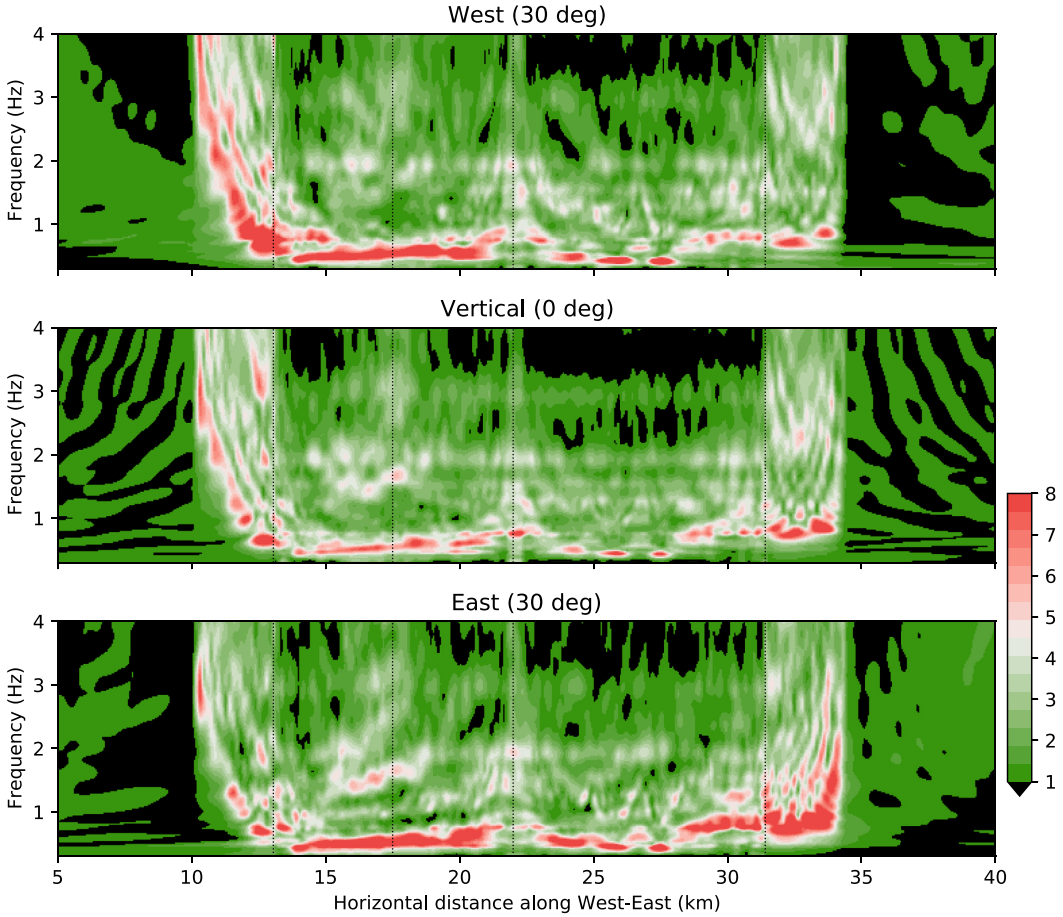

Figure 5. Site-to-rock spectral ratios for different cases of wave incidence. Shown for oblique incidence from west with 30° (top panel), vertical incidence (middle panel), and oblique incidence from east with 30° (bottom panel). We used Northridge input and considered soil non-linearity in all the three cases. Outer and inner dashed lines indicate the basin limits and inner basin sections, respectively.

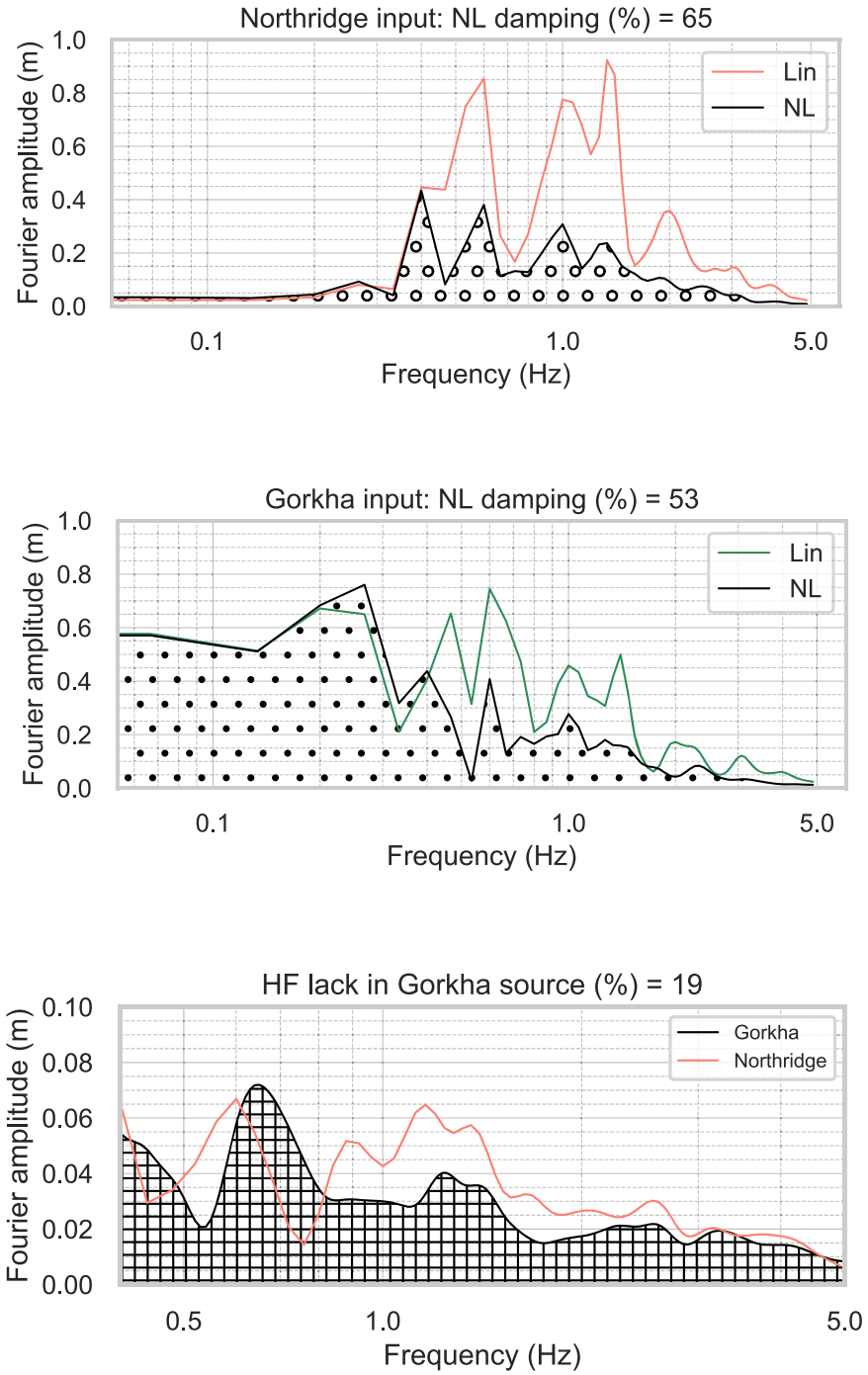

Figure 6. Quantification of high-frequency deficiency due to source and soil non-linearity. Comparison of the Fourier amplitudes of basin ground motion between the elastic and non-linear cases for the use of Northridge (top panel) and Gorkha (middle panel) input and comparison of the Fourier amplitudes of Gorkha and Northridge input motions (bottom panel).

cases lead to smaller spectral ratios and slight reductions of fundamental frequencies compared to the linear simulation. As expected from the discussion in Section 2, the Northridge input case produces stronger non-linearity than the pulse-like case, manifested by slightly smaller fundamental frequencies at certain basin locations (e.g., between 17 and 20 km) and additional damping that changes the spatial pattern of spectral ratios. The spectral ratios at the TVU station (Fig. 4b) show a damping in both non-linear cases up to a factor of 3 with respect to the linear case. The higher non-linearity level in the Northridge case is seen at TVU by slightly smaller spectral ratios above ∼1 Hz. In addition, both non-linear cases produce a slight shift in the resonance frequencies (from 0.5 to 0.45 Hz for TVU), which are comparable to the reported frequency shift values during the Gorkha main shock with respect to aftershocks.

Our further comparisons between the simulations using Gorkha and Northridge inputs support the role of source frequency-content on depletion of high frequency ground motion during the Gorkha earthquake, in addition to soil non-linearity. We performed additional simulations by using as incident input motion the east–west component of the Gorkha event recording at the rock-site station

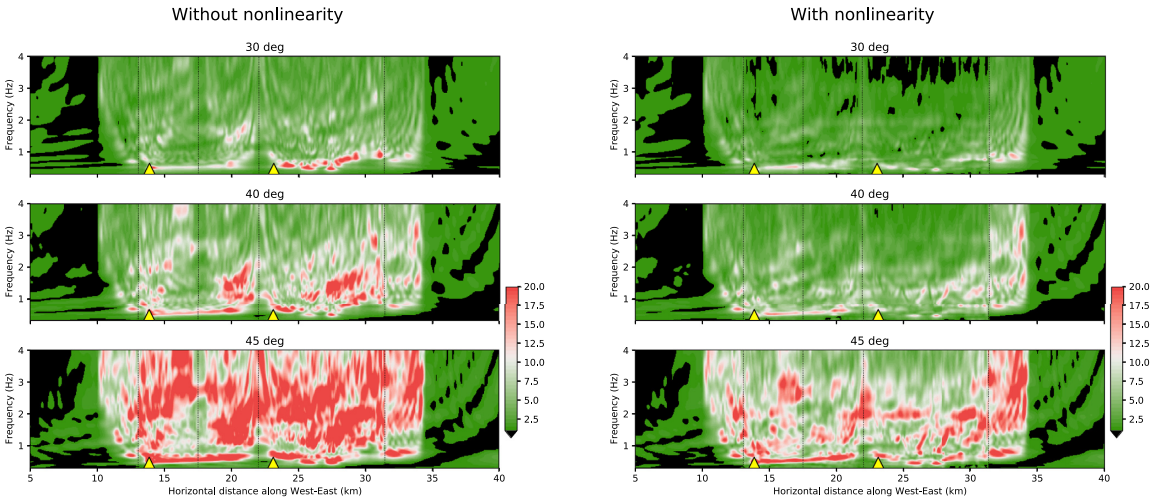

Figure 7. High-frequency ground motion amplification due to the larger wave incidence angle. Site-to-rock spectral ratios for oblique incidence with 30° (top panel), 40° (middle panel) and 45° (bottom panel), for linearity (left-hand panel) and non-linearity (right-hand panel) considerations. Outer and inner dashed lines indicate the basin limits and inner basin sections, respectively. Locations of TVU ($x = 13.8$ km) and THM ($x = 23.1$ km) stations are denoted by triangles.

KTP. For both the Gorkha and Northridge inputs, we first quantify the damping due to soil non-linearity, specifically by calculating the relative change of Fourier spectrum integral of non-linear case with respect to that of the linear case. Details about the chosen time windows to compute the damping percentages are given in SI. Figs 6(a) and (b) shows the ground velocity Fourier amplitudes at the soil station TVU. For both input motions, soil non-linearity causes notable reduction of the ground-motion spectral amplitude above 0.4 Hz, reaching more than 50 per cent reduction relative to the linear case. Second, we quantified the difference of high frequency source content (above 0.4 Hz) between the two cases. In Fig. 6(c), we compare the spectra of the two input motions: The spectral content above 0.4 Hz in the Gorkha case is weaker by roughly 20 per cent compared to the Northridge case. In reality, incident ground motion can further vary due to the fault finiteness. Despite the plane wave assumption here, such a 20 per cent versus 50 per cent partition of the roles of source and soil non-linearity on the high-frequency ground motion depletion underlines the likelihood of the coupled effect of these two factors during the Gorkha earthquake.

On the other hand, despite basin non-linearity, a critically oblique wave incidence can boost the high frequency ground motion (>2 Hz) inside the Kathmandu basin with respect to the outer rock. We performed an additional set of simulations with gradually increased incidence angles and adopting the Northridge input. Fig. 7(a) shows the soil-to-rock spectral ratios in linear simulations with wave incidence angles of 30°, 40° and 45° from east. The basin strongly amplifies ground motion over a broader frequency band at increasing incidence angle. At 40 degrees of incidence, the amplification above 1 Hz is concentrated at the edges of the three sections of the basin, and the soil-to-rock spectral ratio reaches a factor of ∼10 below 5 Hz. At 45 degrees of incidence, the amplification is dramatically larger all over the basin. The theoretical value of refraction due to impedance contrast (by Snell's law) ranges between 20° and 28° for the 1-D simplification of the soil strata. Our additional 2-D simulations probing more incidence angles show that strong broad-band amplification above 2 Hz occurs at incidences higher than ∼42°. For angles larger than this threshold, we found that the change in wave propagation pattern enhances the lateral contrast of ground motion amplitude between sites inside and outside the basin, in favour of a larger high-frequency ground motion inside the basin (detailed in Section S2).

We propose that the incidence angle effect may have contributed to the differences in the response of the Kathmandu basin during past earthquakes, in addition to possible differences of source frequency-content. The 2-D cross-section that we are analysing extends almost parallel to the fault strike of the 2015 earthquake, in the east-west direction (Fig. 1). Given that the rupture propagation was also in this direction during the 2015 earthquake, the real case scenario of the dominant incidence angle and direction is likely to have varied along our 2-D model, differently than our plane wave assumption. Comparing our simulation results with the Gorkha observations, in Fig. 8, the spectral ratios for the incidence of 30° fit better the observations,implying unlikelihood of a large incidence angle (above ∼42°). At TVU station, there is good agreement up to frequencies of ∼2 Hz, and the resonance frequencies are mostly compatible. At THM station, the synthetics overestimate the observation, but the spectral shape is similar up to ∼4 Hz. We interpret the observed weaker spectrum as a result of possible smaller incidence angle and/or higher level of non-linear damping, within the 2-D plane assumption. Moreover, for both incidences the synthetic cases result in larger spectral ratios than the observations above ∼2 Hz. Because the Northridge input has a broader spectrum than the Gorkha source, this result supports the idea that a larger high-frequency amplification could have been observed if the Gorkha source had been richer in that frequency range. We do not have any means to make a similar evaluation for the earlier earthquakes (such as the 1255 and 1934 events) due to the absence of instrumentation at the time, which makes it unclear to assess whether these events are near- or far-field sources. Assuming near-field sources and given that those past earthquakes likely occurred farther from Kathmandu than the 2015 event and yet caused more damages in the Kathmandu basin, the incidence angle deserves to be accounted for in seismic hazard assessment studies for Kathmandu, besides possible source effects.

The results of our study, limited to 2-D *P–SV* wave propagation modelling, suggest opportunities for more complete 3-D mod-

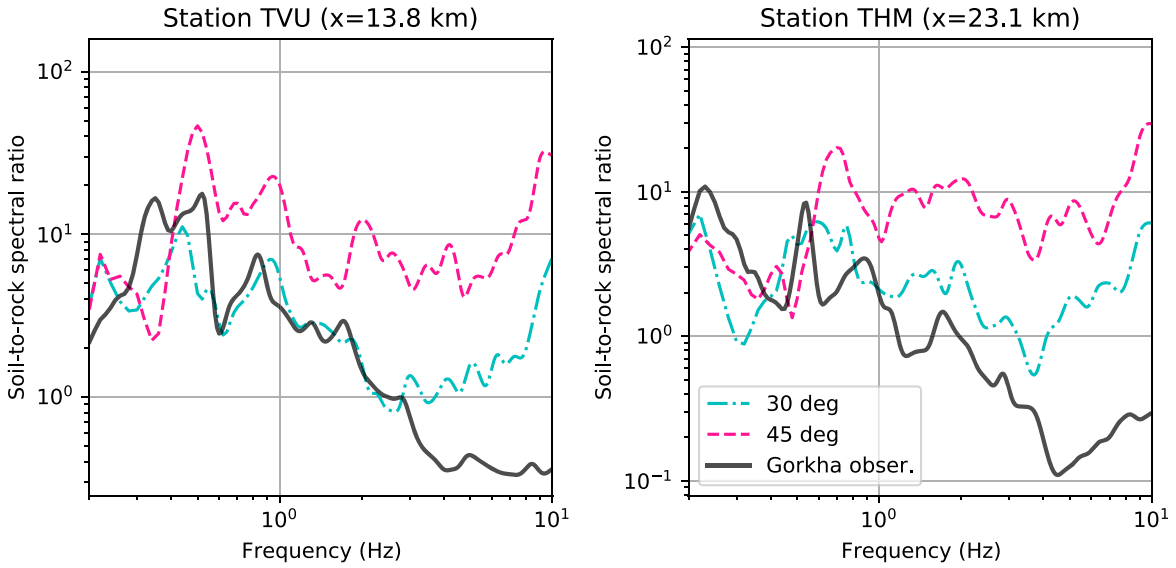

Figure 8. High-frequency ground motion amplification due to wave incidence angle at selected soil stations. Comparison of the soil-to-rock spectral ratios between the cases of 30° and 45°, and the observation during the 2015 Gorkha earthquake, shown for stations TVU (left-hand panel) and THM (right-hand panel), calculated as the ratio of Fourier amplitudes between each station recording and that of KTP rock station.

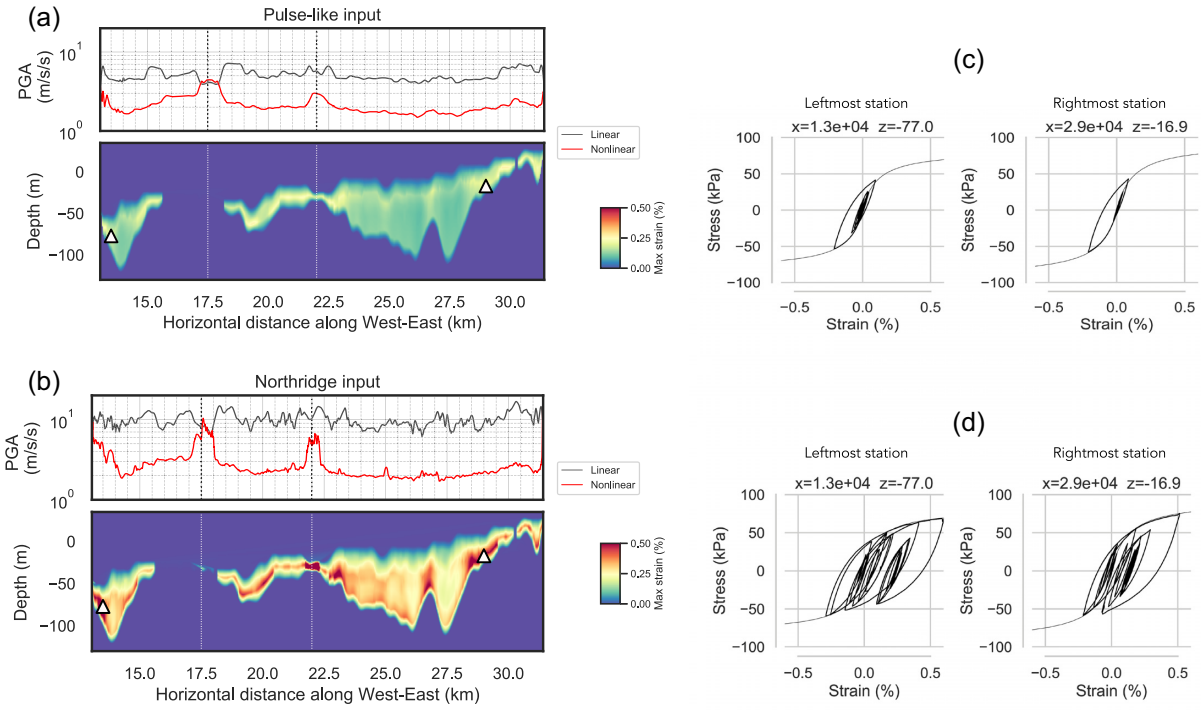

Figure 9. The effect of basin non-linearity on peak ground motion for the two cases of input motion. (a) The comparison of PGA variation along the basin length between linear and non-linear cases (top panel), and maximum strain distribution in the basin (bottom panel), and stress–strain curves at selected basin locations, for the case of Ricker input, (b) same as (a) for the case of Northridge input use. We only show the max. strain values for the non-linear layer and set zero strain elsewhere in the 2-D plots. Selected locations are denoted by triangles in the 2-D plots. Wave incidence is vertical in both cases.

elling. In our additional analyses, comparing 1-D and 2-D modelling along a basin section, we found that 1-D modelling underestimates 2-D ground motion predictions by more than a factor of 10 (Section S3). Similarly, one can expect significant differences between 2-D and 3-D models, because of out-of-plane geometrical features and coupling of *P*, *SV* and *SH* waves that lack in 2-D models. In Fig. S17, we provide exemplary soil-to-spectral ratios for *SH* modelling, and conclude that high-frequency ground motion amplification at larger incidence angle is more pronounced in *P–SV* models. Therefore, we emphasize the necessity to investigate 3-D effects to advance our findings for application in real case studies.

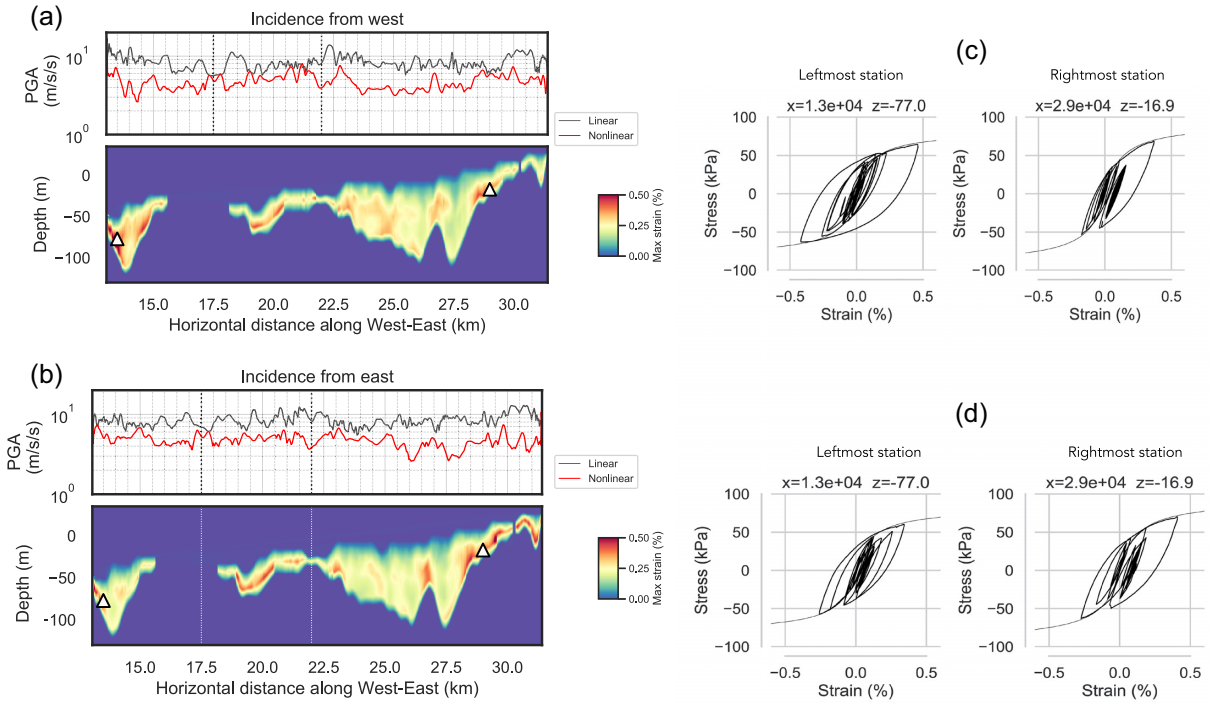

Figure 10. The effect of basin non-linearity on peak ground motion for different wave incidence direction. (a) The comparison of PGA variation along the basin length between linear and non-linear cases (top panel), and maximum strain distribution in the basin (bottom panel), and stress–strain curves at selected basin locations, for the case of wave incidence from west, (b) same as (a) for the case of wave incidence from east. We only show the max. strain values for the non-linear layer and set zero strain elsewhere in the 2-D plots. Selected locations are denoted by triangles in the 2-D plots. The incidence angle equals 30° in both cases.

3.3 Soil non-linearity and oblique wave incidence can sharpen the spatial heterogeneity of ground motion in the basin

The damping effect of soil non-linearity in the Kathmandu basin enhances the contrast of peak ground motion amplitudes between the edges and deeper parts of the basin. We analysed the spatial variation of ground motion amplitudes across the basin and how it relates to the basin non-linearity. Fig. 9 displays the comparison of PGA along the basin length between linear and non-linear cases, together with the maximum—total—strain reached in the non-linear layer. Results are shown for the two input cases: pulse-like (top panel) and Northridge (bottom panel). Wave incidence is vertical in both cases. In the pulse-like input case, the shallower parts close to the basin edges undergo higher strains. In the Northridge input case, the maximum strain is higher everywhere. The stress–strain curves at locations close to eastern and western edges of the basin, Figs 9(b) and (d), show higher complexity of the loading cycle for the Northridge input, consistently with its larger number of zero-crossings (see the discussion in Section 2). For both input motions, in the linear simulations, the PGA values are comparable all along the basin length, although the combined effects of basin geometry and soil stratigraphy lead to slightly larger PGA values close to corners and section boundaries (e.g. at $x = 13$, 15, 18.5, 22 and 30 km). In the simulations with soil non-linearity, PGA is strongly reduced everywhere there is a sufficiently thick non-linear layer below but remains high elsewhere (details in the Supporting Information). The local peaks in the deeper parts of the basin mostly disappear, and the PGA shows notable contrasts near the edges of basin sections favouring larger amplitudes where non-linear soil is not thick. Despite higher level of non-linearity triggered in such thin layers (e.g. $x = 22$ km), the PGA in the proximity remains large, such that the PGA ratio between basin corners and deeper sections can rise to a factor of 5, as seen in the case of Northridge input (at $x = 22$ km versus $x = 25$ km).

The direction of wave incidence can cause further variation of triggered basin non-linearity. Fig. 10 compares the basin response to wave incidence from east and west, for the Northridge input. The incidence angle equals 30° in both cases. Incidence from east results in larger strains in the eastern section. The effect of such higher non-linearity on ground motion is rather slight, manifesting as further local variation of PGA in that section. Incidence from west triggers a similar effect on the western section.

Given that Kathmandu is inhabited by a dense population and hosting highly vulnerable constructions, our findings of the local variation of the ground motion due to the direction of wave incidence and soil non-linearity warrant further research on regional seismic hazard including these factors. Our study is limited to plane wave incidence, and further investigation of the spatial variability of ground motion deserves a closer look into possible effects of source finiteness and rupture directivity.

4 CONCLUSIONS

We found that the Kathmandu basin typically enhances low-frequency ground motion (<2 Hz) with and without non-linear soil behaviour, and regardless of wave incidence angle. This finding supports and expands the insights from past studies of ground motions produced by the 2015 Gorkha earthquake. Here, accounting for the 2-D basin geometry, soil stratigraphy and multi-dimensional

soil non-linearity, thanks to the most recent geotechnical data, we find that low-frequency ground motion amplification in Kathmandu should be expected during future earthquakes.

We also found that the angle of wave incidence can tremendously boost the high-frequency ground motion across an entire basin, compared to bedrock, despite the damping effect of soil non-linearity. In our models, ground motion amplification appears prominently (up to a factor of 5) at wave incidence angles larger than $\sim 42^{\circ}$ relative to vertical. We propose that the position of the source relative to the basin, through the effective wave incidence angle, may have contributed to the differences in damage impact between the Gorkha event and earlier earthquakes. Investigations in broadband to what extent such wave incidence effects prevail when considering 3-D basin effects and finite sources can further advance seismic hazard studies in Kathmandu and other areas.

The spatial variability of ground motion along the Kathmandu basin can be enhanced by basin non-linearity and wave incidence effects. Ground motion can be much stronger near basin edges compared to deeper parts of the basin (up to five times here) due to non-linearity effects. The amplitude and location of amplification is also affected by the direction and angle of incident waves. While the significance of both soil non-linearity and oblique wave incidence is well developed in the literature for simplified sites, as exemplified in Section 1, our analyses on the Kathmandu basin highlight the necessity of considering their coupled effects in seismic hazard assessment studies worldwide on sites with complex basin geometry and soil stratigraphy, such as Los Angeles, Mexico City and Grenoble basins. In that sense, further investigation on the above-mentioned factors can help to better constrain the spatial variability of ground motion in such areas.

DATA AND RESOURCES

All data needed to reproduce this work are available online: 2-D wave propagation modelling tools can be found at https://github.com/jpampuero/sem2dpack. The updates can be followed in the same address.

ACKNOWLEDGMENTS

This work was supported by the French National Research Agency (ANR) through project FAULTS_R_GEMS (grant ANR-17-CE31-0008) and Investments-in-the-Future project UCAJEDI (grant ANR-15-IDEX-01). We acknowledge the comments of the Editor Víctor M. Cruz-Atienza, Kim Olsen and an anonymous reviewer that improved the quality of this manuscript.

REFERENCES

Ampuero, J.-P., 2012. A Spectral Element Method tool for 2D wave propagation and earthquake source dynamics User's Guide, https://sourceforge.net/projects/sem2d/.

Ampuero, J.-P., Vilotte, J.-P. & Sanchez-Sesma, F., 2002. Nucleation of rupture under slip dependent friction law: simple models of fault zone, *J. geophys. Res.,* **107**(B12), ESE 2–1-ESE 2-19.

Asimaki, D., Mohammadi, K., Mason, H.B., Adams, R.K., Rajaure, S. & Khadka, D., 2017. Observations and simulations of basin effects in the kathmandu valley during the 2015 Gorkha, Nepal, earthquake sequence, *Earthq. Spectra,* **33**(Suppl 1), 35–53.

Auden, J. & Ghosh, A., 1935. Preliminary account of the earthquake of the 15th January, 1934, in Bihar and Nepal, *Record. Geol. Survey India,* **68**(2), 177–239.

Avouac, J.-P., Meng, L., Wei, S., Wang, T. & Ampuero, J.-P., 2015. Lower edge of locked Main Himalayan Thrust unzipped by the 2015 Gorkha earthquake, *Nat. Geosci.,* **8**(9), 708–711.

Ayoubi, P., Asimaki, D. & Mohammdi, K., 2018. Basin effects in strong ground motion: a case study from the 2015 Gorkha, Nepal, Earthquake, in *Geotechnical Earthquake Engineering and Soil Dynamics V: Seismic Hazard Analysis, Earthquake Ground Motions, and Regional-Scale Assessment,* pp. 288–296, American Society of Civil Engineers Reston.

Ayoubi, P., Mohammadi, K. & Asimaki, D., 2021. A systematic analysis of basin effects on surface ground motion, *Soil Dyn. Earthq. Eng.,* **141,** doi:10.1016/j.soildyn.2020.106490.

Bard, P.-Y. *et al.*, 1995. Effects of surface geology on ground motion: recent results and remaining issues, in *Proceedings of the 10th European conference on earthquake engineering,* Vienna, Austria, pp. 305–323, Rotterdam.

Bonilla, L.F., Gélis, C. & Régnier, J., 2011. The challenge of nonlinear site response: field data observations and numerical simulations, in *Proceedings of the Effects of Surface Geology on Seismic Motion,* August 23–26, 2011, University of California, Santa Barbara, CA.

Castro-Cruz, D., Regnier, J., Bertrand, E. & Courboulex, F., 2020. A new parameter to empirically describe and predict the non-linear seismic response of sites derived from the analysis of Kik-Net database, *Soil Dyn. Earthq. Eng.,* **128,** doi:10.1016/j.soildyn.2019.105833.

Chaljub, E., Komatitsch, D., Vilotte, J.-P., Capdeville, Y., Valette, B. & Festa, G., 2007. Spectral-element analysis in seismology, *Adv. Geophys.,* **48,** 365–419.

Chen, G., Jin, D., Zhu, J., Shi, J. & Li, X., 2015. Nonlinear analysis on seismic site response of Fuzhou Basin, China, *Bull. seism. Soc. Am.,* **105**(2A), 928–949.

Chen, M. & Wei, S., 2019. The 2015 Gorkha, Nepal, earthquake sequence: II. Broadband simulation of ground motion in Kathmandu, *Bull. seism. Soc. Am.,* **109**(2), 672–687.

Chiaro, G., Kiyota, T., Pokhrel, R.M., Goda, K., Katagiri, T. & Sharma, K., 2015. Reconnaissance report on geotechnical and structural damage caused by the 2015 Gorkha Earthquake, Nepal, *Soils Found.,* **55**(5), 1030–1043.

Clayton, R. & Engquist, B., 1977. Absorbing boundary conditions for acoustic and elastic wave equations, *Bull. seism. Soc. Am.,* **67**(6), 1529–1540.

Dal Zilio, L., van Dinther, Y., Gerya, T. & Avouac, J.-P., 2019. Bimodal seismicity in the Himalaya controlled by fault friction and geometry, *Nat. Commun.,* **10**(1), 1–11.

De Luca, G., Marcucci, S., Milana, G. & Sano, T., 2005. Evidence of low-frequency amplification in the city of L'Aquila, Central Italy, through a multidisciplinary approach including strong-and weak-motion data, ambient noise, and numerical modeling, *Bull. seism. Soc. Am.,* **95**(4), 1469–1481.

Dixit, A.M., Yatabe, R., Dahal, R.K. & Bhandary, N.P., 2013. Initiatives for earthquake disaster risk management in the Kathmandu Valley, *Nat. Hazards,* **69**(1), 631–654.

Esmaeilzadeh, A., Motazedian, D. & Hunter, J., 2019. 3D nonlinear ground-motion simulation using a physics-based method for the Kinburn basin, *Bull. seism. Soc. Am.,* **109**(4), 1282–1311.

Frankel, A.D., Carver, D.L. & Williams, R.A., 2002. Nonlinear and linear site response and basin effects in Seattle for the M 6.8 Nisqually, Washington, earthquake, *Bull. seism. Soc. Am.,* **92**(6), 2090–2109.

Galetzka, J. *et al.*, 2015. Slip pulse and resonance of the Kathmandu basin during the 2015 Gorkha earthquake, Nepal, *Science,* **349**(6252), 1091–1095.

Gélis, C. & Bonilla, L.F., 2012. 2-DP–SV numerical study of soil–source interaction in a non-linear basin, *Geophys. J. Int.,* **191**(3), 1374–1390.

Gilder, C.E. *et al.*, 2020. The SAFER geodatabase for the Kathmandu Valley: geotechnical and geological variability, *Earthq. Spectra,* **36**(3), 1549–1569.

Hashash, Y. *et al.*, 2015. Geotechnical field reconnaissance: Gorkha (Nepal) earthquake of April 25, 2015 and related shaking sequence, Geotechnical extreme event reconnaisance GEER association. Report No. GEER-040.

Hough, S.E. & Roger, B., 2008. Site response of the Ganges basin inferred from re-evaluated macroseismic observations from the 1897 Shillong,

1905 Kangra, and 1934 Nepal earthquakes, *J. Earth Syst. Sci.,* **117**(2), 773–782.

Hough, S.E., Martin, S.S., Gahalaut, V., Joshi, A., Landes, M. & Bossu, R., 2016. A comparison of observed and predicted ground motions from the 2015 Mw 7.8 Gorkha, Nepal, earthquake, *Nat. Hazards,* **84**(3), 1661–1684.

Iwan, W.D., 1967. On a class of models for the yielding behavior of continuous and composite systems, *J. Appl. Mech. ,* **34**(3), 612–617.

Japan International Cooperation Agency (JICA), Ministry of Home Affairs, His Majesty's Government of NepaL. 2002. The study on earthquake disaster mitigation in the Kathmandu Valley, Kingdom of Nepal, Final Report, Vol. 1, Nippon Koei Co., Ltd. Oyo Corporation, Tokyo.

Joyner, W.B., 1975. A method for calculating nonlinear seismic response in two dimensions, *Bull. seism. Soc. Am.,* **65**(5), 1337–1357.

Kaushik, H., Bevington, J., Jaiswal, K., Lizundia, B. & Shrestha, S., 2016. Buildings (EERI earthquake reconnaissance team report: M7. 8 Gorkha, Nepal earthquake on April 25, 2015 and its aftershocks), Tech. rep., Earthquake Engineering Research Institute.

Komatitsch, D. & Vilotte, J.-P., 1998. The spectral element method: an efficient tool to simulate the seismic response of 2D and 3D geological structures, *Bull. seism. Soc. Am.,* **88**(2), 368–392.

Laurendeau, A. *et al.*, 2017. Low-frequency seismic amplification in the Quito Basin (Ecuador) revealed by accelerometric recordings of the RENAC Network, *Bull. seism. Soc. Am.,* **107**(6), 2917–2926.

Liu, S., Datta, S., Bouden, M. & Shah, A., 1991. Scattering of obliquely incident seismic waves by a cylindrical valley in a layered half-space, *Earthq. Eng. Struct. Dyn.,* **20**(9), 859–870.

Marsh, J., Larkin, T., Haines, A. & Benites, R., 1995. Comparison of linear and nonlinear seismic responses of two-dimensional alluvial basins, *Bull. seism. Soc. Am.,* **85**(3), 874–889.

Michel, S., Avouac, J.-P., Lapusta, N. & Jiang, J., 2017. Pulse-like partial ruptures and high-frequency radiation at creeping-locked transition during megathrust earthquakes, *Geophys. Res. Lett.,* **44**(16), 8345–8351.

Olsen, K., 2000. Site amplification in the Los Angeles basin from three-dimensional modeling of ground motion, *Bull. seism. Soc. Am.,* **90**(6B), S77–S94.

Olsen, K., Day, S. & Bradley, C., 2003. Estimation of Q for long-period (>2 sec) waves in the Los Angeles basin, *Bull. seism. Soc. Am.,* **93**(2), 627–638.

Oral, E., 2016. Modélisation multi-dimensionnelle de la propagation des ondes sismiques dans des milieux linéaires et non-linéaires, *PhD thesis*, Paris Est.

Oral, E., Gélis, C., Bonilla, L.F. & Delavaud, E., 2017. Spectral element modelling of seismic wave propagation in visco-elastoplastic media including excess-pore pressure development, *Geophys. J. Int.,* **211**(3), 1494–1508.

Oral, E., Gélis, C. & Bonilla, L.F., 2019. 2-D P-SV and SH spectral element modelling of seismic wave propagation in non-linear media with pore-pressure effects, *Geophys. J. Int.,* **217**(2), 1353–1365.

Papageorgiou, A.S. & Kim, J., 1993. Propagation and amplification of seismic waves in 2-D valleys excited by obliquely incident P-and SV-waves, *Earthq. Eng. Struct. Dyn.,* **22**(2), 167–182.

Piya, B.K., 2004. Generation of a Geological database for the liquefaction hazard assessment in Kathmandu Valley, *Master's thesis*, International Institute of Geo-Information Science and Earth Observation, Enschede, the Netherlands.

Psarropoulos, P., Tazoh, T., Gazetas, G. & Apostolou, M., 2007. Linear and nonlinear valley amplification effects on seismic ground motion, *Soils Found.,* **47**(5), 857–871.

Ragozzino, E., 2014. Nonlinear seismic response in the western L'Aquila basin (Italy): numerical FEM simulations vs. ground motion records, *Eng. Geol.,* **174,** 46–60.

Rajaure, S. *et al.*, 2017. Characterizing the Kathmandu Valley sediment response through strong motion recordings of the 2015 Gorkha earthquake sequence, *Tectonophysics,* **714,** 146–157.

Régnier, J. *et al.*, 2018. PRENOLIN: International benchmark on 1D nonlinear site-response analysis—validation phase exercise, *Bull. seism. Soc. Am.,* **108**(2), 876–900.

Roten, D., Olsen, K., Day, S., Cui, Y. & Fäh, D., 2014. Expected seismic shaking in Los Angeles reduced by San Andreas fault zone plasticity, *Geophys. Res. Lett.,* **41**(8), 2769–2777.

Sakai, H., 2001. Stratigraphic division and sedimentary facies of the Kathmndu Basin Group, central Nepal, *J. Nepal Geol. Soc.,* **25**(1), 19–32.

Sakai, H., Fuji, R. & Kuwahara, Y., 2002. Changes in the depositional system of the Paleo-Kathmandu Lake caused by uplift of the Nepal Lesser Himalayas, *J. Asian Earth Sci.,* **20**(1), 267–276.

Sapkota, S., Bollinger, L., Klinger, Y., Tapponnier, P., Gaudemer, Y. & Tiwari, D., 2013. Primary surface ruptures of the great Himalayan earthquakes in 1934 and 1255, *Nat. Geosci.,* **6**(1), 71–76.

Singh, D. & Gupta, H.K., 1980. Source dynamics of two great earthquakes of the Indian subcontinent: the Bihar-Nepal earthquake of January 15, 1934 and the Quetta earthquake of May 30, 1935, *Bull. seism. Soc. Am.,* **70**(3), 757–773.

Takai, N., Shigefuji, M., Rajaure, S., Bijukchhen, S., Ichiyanagi, M., Dhital, M.R. & Sasatani, T., 2016. Strong ground motion in the Kathmandu Valley during the 2015 Gorkha, Nepal, earthquake, *Earth, Planets Space,* **68**(1), 1–8.

Wang, Y., Day, S.M. & Denolle, M.A., 2019. Geometric controls on pulse-like rupture in a dynamic model of the 2015 Gorkha earthquake, *J. geophys. Res.,* **124**(2), 1544–1568.

Wei, S., Chen, M., Wang, X., Graves, R., Lindsey, E., Wang, T., Karakaş, Ç. & Helmberger, D., 2018. The 2015 Gorkha (Nepal) earthquake sequence: I. Source modeling and deterministic 3D ground shaking, *Tectonophysics,* **722,** 447–461.

Zhang, H., Van Der Lee, S. & Ge, Z., 2016. Multiarray rupture imaging of the devastating 2015 Gorkha, Nepal, earthquake sequence, *Geophys. Res. Lett.,* **43**(2), 584–591.

Zhang, N., Gao, Y. & Pak, R.Y., 2017. Soil and topographic effects on ground motion of a surficially inhomogeneous semi-cylindrical canyon under oblique incident SH waves, *Soil Dyn. Earthq. Eng.,* **95,** 17–28.

Zhu, C., Thambiratnam, D.P. & Zhang, J., 2016. Response of sedimentary basin to obliquely incident SH waves, *Bull. Earthq. Eng.,* **14**(3), 647–671.

Delavaud, E., Cupillard, P., Festa, G. & Vilotte, Jean-Pierre, 2006. 3D spectral element method simulations of the seismic response in the Caracas basin, *Third International Symposium on the Effects of Surface Geology on Seismic Motion,* **1,** 512–522.

SUPPORTING INFORMATION

Supplementary data are available at *GJI* online.

Figure S1. Observational constraints on the non-linear rheology. Top left-hand panel: observed frequency shift versus PGA during the 2015 sequence (Rajaure *et al*. 2017) and curve fitted according to the non-linear rheology model. Top right-hand panel: backbone curve corresponding to the fitted curve. Bottom panel: reference strain in the non-linear layer in our numerical models, normalized by the overall maximum reference strain indicated in the subplot title.

Figure S2. Gorkha input used in the simulations. Velocity–time histories in units of m s^{-1} (left-hand panel), and corresponding Fourier amplitude (right-hand panel).

Figure S3. Top panel: ground velocity time histories at TVU station ($x \sim 13.865$ km) for linear and non-linear models with the Gorkha input. Bottom panel: relative damping level (in percentage) due to soil non-linearity.

Figure S4. Same as Fig. S3 but for simulations with the Northridge input.

Figure S5. High-frequency ground motion amplification due to larger wave incidence angle. Site-to-rock spectral ratios for oblique wave incidence with 40 (top panel), 42 (middle panel) and 45° (bottom panel) relative to vertical, for linear rheology. We used pulse-like input motion in all the three cases. Vertical dashed lines indicate the limits of the basin and its inner sections.

Figure S6. PGA variation inside the basin for linear (top panel) and non-linear (bottom panel) rheologies. The wave incidence is vertical and the input wave is pulse-like. PGA remains relatively large close to basin edges where the non-linear soil layer is thinner, such as near $x = 17.5$ km $x = 22.5$ km and $x = 30$km.

Figure S7. Same as Fig. S1(bottom panel) but for a non-linear soil with friction angle of 28°.

Figure S8. Effect of changing soil friction angle on basin non-linear strain and ground motion. (a) Distribution of PGA along the basin (top panel) maximum strain distribution inside the basin (bottom panel) for the preferred non-linear model with a friction angle of 10°. (b) Same as (a) but for a friction angle of 28°. (c) Stress–strain curves for both models at selected locations near the west (left-hand panel) and east (right-hand panel) ends of the basin, indicated by triangles in (a, b) bottom. We used pulse-like input motion and vertical incidence in both cases.

Figure S9. Same as Fig. 7(right-hand panel) but for a non-linear soil with friction angle of 28°.

Figure S10. (a) Fourier amplitude of the geometric mean of horizontal rock motion for the cases of 30° and 45°, and of the horizontal input motion for each case. Fourier amplitude of ground motion at the basin station TVU (b) and THM (c). In all cases, the input is pulse-like and the soil rheology is non-linear.

Figure S11. Fourier amplitude of selected rock motion outside the basin for three different incidence angles, located at $x = 8$ km (left-hand panel) and $x = 36$ km (right-hand panel).

Figure S12. Velocity time histories of the selected rock motion outside the basin for three different incidence angles, located at $x = 8$ km (top panel) and $x = 36$ km (bottom panel).

Figure S13. Same as Fig. S10 but for vertical ground motions.

Figure S14. Comparison of velocity–time histories between 1-D and 2-D linear models, shown for horizontal (top panel) and vertical (bottom panel) directions. Input is pulse-like, and wave incidence is vertical, in both models.

Figure S15. Same as Fig. S14 for non-linearity.

Figure S16. Comparison between 1-D and 2-D models of stress-strain curves for a selected station, during (left-hand panel) and after (right-hand panel) the initial 9 s of wave propagation.

Figure S17. Same as Fig. 7(left-hand panel) for *SH*-wave propagation model.

Figure S18. Comparison of soil-to-rock spectral ratios at two selected stations between different rheology models and observations, for stations TVU (left-hand panel) and THM (right-hand panel).

Figure S19. Odograms of velocity time histories at different depths for the case of vertical incidence. Input motion is pulse-like and we consider non-linearity. Time is shown with colour in units of seconds.

Figure S20. Same as Fig. S19, for an incidence angle of 45°.

Figure S21. Triggered soil non-linearity for the case of vertical incidence. Number of activated plasticity surfaces (top row), temporal change of strain (second row) and horizontal (third row) and vertical (bottom row) velocities.

Figure S22. Same as Fig. S21 but for the case of incidence angle of 45°.

Figure S23. Same as Fig. S21, for the Northridge input.

Figure S24. Same as Fig. S22, for the Northridge input.

Please note: Oxford University Press is not responsible for the content or functionality of any supporting materials supplied by the authors. Any queries (other than missing material) should be directed to the corresponding author for the paper.